Multistability, Noise Induced Transitions, and Stochastic Resonance in a Nonlinear Oscillator With a Nonvolatile Memristor

Multistability, Noise Induced Transitions, and Stochastic Resonance in a Nonlinear Oscillator With a Nonvolatile Memristor

Kailing Song, *Member, IEEE*, Michele Bonnin, Alon Ascoli, *Senior Member, IEEE*, and Fernando Corinto, *Senior Member, IEEE*

***Abstract*—We investigate multistability, noise-induced transitions, and stochastic resonance in a second-order nonlinear oscillator incorporating a nonvolatile memristive device. The memristor provides a programmable nonlinear conductance, enabling bistable dynamics with two asymptotically stable equilibrium points separated by a saddle. Under periodic excitation, the system exhibits coexisting limit cycles, period-doubling cascades, boundary crises, and transitions to chaos. Lyapunov exponent analysis reveals repeated crossings of the edge-of-chaos regime, where the largest nonzero exponent approaches zero, marking a balance between stability and sensitivity to perturbations. The effects of additive Gaussian white noise are analyzed by reformulating the dynamics in terms of an effective potential landscape, where noise induces random transitions between coexisting attractors. Transition rates are accurately described in the weak-noise regime by the Eyring–Kramers formula. When periodic forcing and noise act jointly, the system exhibits stochastic resonance, with optimal synchronization occurring when the forcing period matches the mean noise-induced transition time. These results demonstrate that memristor-based nonlinear circuits naturally operate near critical dynamical regimes and provide a compact hardware platform for studying noise-assisted computation and edge-of-chaos dynamics in neuromorphic systems.**

***Index Terms*—Memristor, multistability, Gaussian white noise, noise induced transitions, stochastic resonance.**

I. Introduction

IN THE theory of dynamical systems, multistability denotes the coexistence of two or more stable limit sets. In systems that admit an energy function, these stable states correspond to local minima of the associated energy landscape, separated by barriers that prevent spontaneous transitions. More generally, limit sets may take the form of equilibrium points, limit cycles, quasi-periodic orbits, or strange attractors.

A limit set is said to be attractive (or asymptotically stable) when trajectories in its vicinity not only remain close but converge to the set itself. In multistable systems, the basins of attraction of distinct attractors are separated by invariant manifolds known as separatrices. Examples include the stable manifolds of saddle points, close to which trajectories are transiently attracted toward the saddle before being repelled along its unstable manifold.

Dynamical systems exhibiting multiple attractors have long provided a theoretical framework for understanding how neural dynamics can support computation, memory, and decision-making. In attractor-based models of decision making, distinct stable states represent alternative choices, and competition among neuronal populations drives the network toward one of these states [1]. Such dynamics enable recurrent cortical circuits to implement winner-take-all mechanisms.

Empirical evidence supports this framework: during perceptual decision tasks, neural activity often exhibits delayed and abrupt transitions between discrete attractor states. These transitions have been observed during taste processing (where the decision is between ingesting or expelling a tastant) [2], in somatosensory discrimination tasks [3], and in motion direction detection [4]. Alternative analyses have identified gradual ramping activity during stimulus accumulation, with sudden transitions corresponding to changes of mind. In certain model variants, the undecided state itself constitutes a metastable attractor, allowing decisions to emerge through noise-induced transitions [5].

Spatial navigation, e.g. the process by which an animal (or agent) maps, represents, and moves through space, provides another strong biological evidence for attractor-based dynamics in neural systems. Networks of head-direction cells and grid cells in the mammalian brain maintain stable representations of orientation and position through continuous attractor mechanisms [6].

A continuous attractor network can support continuous spatial representations, such as smoothly varying head direction, or position in space. In these models, the neural state evolves along a low-dimensional manifold (for example, a ring or torus) as the agent moves. In cases of ambiguous spatial information, when there may be competing hypotheses about where the agent is, the network could switch between different attractors, transiently occupy one or another, or maintain mixtures, until sensory inputs resolve the ambiguity [7].

Received 24 December 2025; revised 13 March 2026 and 14 April 2026; accepted 15 April 2026. This work was supported in part by the Deutsche Forschungsgemeinschaft (DFG) project "Recommend: REservoir COMputing with MEmristive Nonlinear Dynamics: Theory, Design and Applications," in part by the ICS (Made in Italy – Circular and Sustainable) Extended Partnership, and in part by the European Union Next-Generation EU (PIANO NAZIONALE DI RIPRESA E RESILIENZA (PNRR) – MISSIONE 4 COMPONENTE 2, INVESTIMENTO 1.3 – D.D. 1551.11-10-2022, PE00000004). This article was recommended by Associate Editor V. Lanza. *(Corresponding author: Michele Bonnin.)*

The authors are with the Department of Electronics and Telecommunications, Politecnico di Torino, 10129 Turin, Italy (e-mail: michele.bonnin@polito.it).

Digital Object Identifier 10.1109/TCSI.2026.3685449

Persistent activity in the prefrontal cortex has likewise been interpreted as the stabilization of neural dynamics into an attractor state that maintains information over time [8]. Analyses of simultaneously recorded neuronal ensembles have revealed transitions between discrete, metastable activity states in premotor and prefrontal cortex during spatial working-memory tasks [9], as well as in gustatory cortex during taste processing [10]. The timing of such transitions correlates with ongoing behavior and can predict subsequent responses [11].

Hopfield pioneered the idea of exploring the complex energy landscape of Artificial Neural Networks (ANNs) to implement associative memory and pattern recognition [12]. In such networks, memories are encoded as point attractors within an energy landscape. When presented with a noisy or incomplete cue, the network converges to the corresponding attractor, thereby performing content-addressable memory retrieval. Since this seminal work, ANNs have played a central role in associative memory [13], [14], pattern recognition [15], deep learning [16], [17], intelligent control [18], [19], and many other domains.

Recurrent neural networks (RNNs) must be monostable when solving single-objective optimization problems [20], [21]; otherwise, multiple equilibrium points can produce spurious, suboptimal responses. Conversely, solving multi-objective optimization problems requires RNNs with multiple equilibrium points, where the number of equilibria determines the system's capacity for pattern recognition and associative memory [22]. In reservoir computing and echo state networks, transient trajectories approach attractors, and computation is extracted from these dynamics [23]. More recently, deep recurrent networks have been analyzed using dynamical systems tools to reveal how attractors represent categories, rules, and sequences [24].

ANNs were originally developed to emulate biological learning mechanisms. However, they are typically implemented on von Neumann architectures, which lack many of the advantages of brain computation, such as massive parallelism, low energy consumption, fault tolerance, and inherent robustness [25]. This limitation led to the development of neuromorphic computing, a field that seeks to reproduce the brain's computational principles using physical devices. The implementation of spiking neural networks (SNNs) on neuromorphic hardware, grounded in biological processing principles, provides a promising path toward adaptive and energy-efficient artificial intelligence (AI) systems [26], [27], [28]. This approach, driven by advances in materials science, device physics, chip integration, and neuroscience, has attracted significant interest from both neuroscientists and computer scientists.

Within the neuromorphic paradigm, multistability can emerge at the single neuron level, where certain types of artificial neurons can exist in a repetitively firing state, a bursting state or a quiescent state [14], [29], and at a macro level, where entire neuronal network configurations can coexist, in which dynamical neuronal clusters are uniquely connected to perform different operations [30], [31].

A central enabler of neuromorphic architectures is memristor technology, which provides a compact, energy-efficient, and inherently analog means of emulating synaptic plasticity. A memristor (memory resistor) is a two-terminal electronic device whose resistance depends on the history of charge flow through it. This property allows it to store information in its conductance state, closely resembling the adaptive weight of a biological synapse. By modulating their conductance through voltage or current pulses, memristors naturally implement synaptic learning rules such as spike-timing-dependent plasticity, enabling local and online adaptation without explicit memory and processor separation [32].

Memristor-based neuromorphic systems integrate memory and computation within the same physical substrate, thereby overcoming the bandwidth and energy bottlenecks of conventional von Neumann architectures. Large-scale memristive crossbar arrays can efficiently perform parallel matrix–vector multiplications—the core operation of neural networks—using Ohm's and Kirchhoff's laws. Such hardware not only accelerates computation but also offers non-volatility, scalability, and high integration density.

Recent developments have demonstrated hybrid CMOS–memristor circuits capable of implementing spiking networks, associative memories, and even dynamic attractor behaviors, where memristive elements act as both storage and adaptive components [33], [34], [35]. As fabrication technologies mature, memristor-based neuromorphic hardware is expected to play a central role in building energy-efficient, brain-inspired computing systems capable of real-time learning and robust information processing.

In this work, we present a theoretical investigation of the nonlinear and stochastic dynamics of a memristor-based oscillator incorporating an experimentally characterized non-volatile RRAM nonlinearity. The proposed circuit serves as a physically grounded dynamical system in which multistability, bifurcation phenomena, and noise-driven effects can be systematically analyzed.

Our work aims to advance the development of brain-like machines. By exploiting multistability, noise-induced transitions, and stochastic resonance, it is possible to design innovative bio-mimetic sensors that leverage the interplay between a well-defined periodic stimulus and a noise source of internal or external origin. Such dynamically rich cells, incorporating non-volatile memristors with fading memory, can detect low-amplitude signals that would otherwise remain imperceptible.

The memristive circuit proposed here, despite its simplicity, exhibits complex dynamic behavior, including multistability, edge-of-chaos dynamics, noise-induced transitions, and stochastic resonance. This makes it a suitable platform for exploring applications in reservoir computing and a benchmark for neuromorphic systems in tasks such as decision-making, motion detection, and spatial navigation. Its ability to switch between different attractors not only enhances the resolution of ambiguous inputs but also supports multi-objective optimization, analogous to stochastic gradient descent in artificial learning systems, making it particularly valuable for adaptive, noise-sensitive computations.

In Section II, we describe the physical implementation of the memristor. In Section III, we derive a normalized

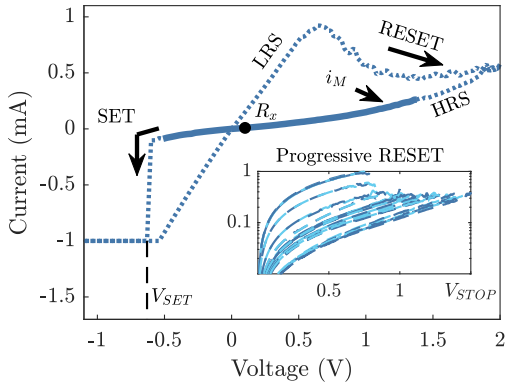

Fig. 1. Switching operation of the Pt/HfO_2/TiN nonvolatile memristive device. The thick line highlights the v–i characteristic in the HIGH resistive state, which is used in the oscillator circuit.

state-space model and characterize the autonomous dynamics of the second-order oscillator including the nonvolatile memristor. We identify equilibrium points, stability properties, and the separatrix delimiting the basins of attraction of the different invariant sets. We study the periodically forced system in Section IV, establishing the occurrence of coexisting limit cycles, period-doubling cascades, boundary crises, and transitions to chaos, which are rigorously characterized through Lyapunov exponent analysis and bifurcation structures in the parameter space. The effect of stochastic perturbations is subsequently addressed in Section V. By formulating an equivalent stochastic dynamical model and introducing an effective potential, we provide an analytical interpretation of noise-induced transitions.

Finally, we analyze the interplay between periodic forcing and noise, demonstrating the emergence of stochastic resonance and identifying the associated matching condition. The theoretical results provide fundamental insight into edge-of-chaos operation in memristor-based nonlinear circuits and establish a foundation for their use in neuromorphic and reservoir computing architectures. Section VI is devoted to conclusions.

II. Physical Implementation of the RRAM Device

We investigate resistive random-access memory (RRAM) devices consisting of 50 nm Pt / 5.5 nm HfO2 / 40 nm TiN stacks, with an active area of $40 \times 40\ \mu m^2$. The fabrication process and modeling methodology are described in detail in [36] and [37]. After an appropriate electroforming step, the device exhibits a well-defined resistive switching behavior. Fig. 1 shows a representative bipolar v–i switching cycle. Starting from the low-resistance state (LRS), the device undergoes a RESET transition to the high-resistance state (HRS) upon application of a positive voltage ($V_{\mathrm{RESET}} = 2.65$ V). Conversely, applying a suitable negative voltage (V_{SET}) under current compliance induces the SET transition, abruptly returning the device to the low-resistance state. The terms LRS and HRS (also referred to as LOW and HIGH, respectively) denote the states of the device following the SET and RESET operations.

The v–i characteristics in the HIGH resistive state are strongly nonlinear. A polynomial fit of the measured data shows that the relationship can be modeled as a fifth-order polynomial:

$$i_N(v) = \sum_{k=1}^{5} G_k\, v^k, \tag{1}$$

where the conductance coefficients G_k take different values upon programming the nonvolatile memristive device. The values used here, corresponding to a selected HIGH resistive state, are: $G_1 = 1.91\,\mu$S, $G_2 = 0.31\,\mu$S/V, $G_3 = 19.1\,\mu$S/V^2, $G_4 = -5.2\,\mu$S/V^3 and $G_5 = 1.77\,\mu$S/V^4.

The choice of a fifth-degree polynomial reflects a balance between accuracy and model complexity. Higher-order terms have negligible coefficients and do not significantly affect the circuit dynamics within the voltage range where the memristor operates as a low conductance resistor. Moreover, complex nonlinear phenomena such as multistability, bifurcations, and chaos, arise already from low-order (quadratic and cubic) nonlinearities, as shown in classical systems like the van der Pol oscillator, the Lorenz system, and Chua's circuit.

III. Memristor Based Nonlinear Oscillator

We have used the RRAM device to implement a programmable nonlinear resistor in a second order nonlinear oscillator, shown in Fig. 2. The circuit is composed of two reactive elements, an inductor and a capacitor, connected in series with a linear resistor. A voltage source is included, to model external stimuli. A shunted resistor, characterized by negative conductance[1] ($G < 0$) is connected in parallel with the nonvolatile memristive element, that provides the nonlinearity thanks to its $v - i$ characteristic.

Applying Kirchhoff's laws yields the following system of state equations:

$$\frac{di}{dt} = -\frac{R}{L}i - \frac{1}{L}v + \frac{1}{L}v_s(t) \tag{2a}$$

$$\frac{dv}{dt} = \frac{1}{C}(i - Gv) - \frac{1}{C}i_N(v), \tag{2b}$$

where i and v denote the state variables, and $i_N(v)$ is defined in (1). The parameter values used in the analysis are $R = 49.820$ kΩ, $L = 24.82$ H, $C = 10$ nF, and $G = 33.893\ \mu$S.

Introducing the normalized voltages $x_1 = R\,i$ and $x_2 = v$, and the normalized time $t' = t/\tau$, where $\tau = RC$ is a time constant, Eq. (2) can be rewritten as

$$\frac{dx_1}{dt'} = -\frac{R^2C}{L}(x_1 + x_2) + \frac{R^2C}{L}\,v_s(\tau\, t') \tag{3a}$$

$$\frac{dx_2}{dt'} = (x_1 - R\,G\,x_2) - R\,i_N(x_2). \tag{3b}$$

For the chosen parameter values, we have $R^2C/L = 1$. Introducing the dimensionless parameter $\rho = RG$ and $f(x_2) = R\,i_N(x_2)$, the normalized equations take the form

$$\frac{dx_1}{dt} = -(x_1 + x_2) + v_s(\tau\, t) \tag{4a}$$

$$\frac{dx_2}{dt} = x_1 - \rho x_2 - f(x_2), \tag{4b}$$

[1]A negative resistance can be synthesized via a classical Negative Impedance Converter.

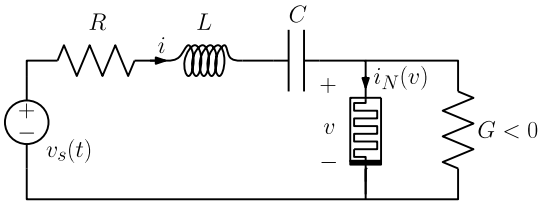

Fig. 2. Second order circuit with nonvolatile memristive device.

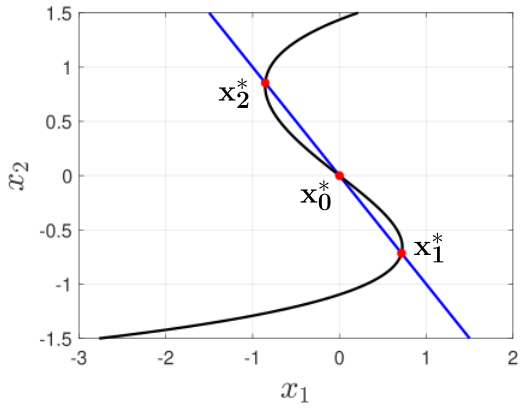

Fig. 3. Nullclines showing the locations of the equilibrium points.

where, with a little abuse of notation, we made the substitution $t' \to t$ for simplicity.

A systematic bifurcation analysis with respect to the internal parameters, such as the coefficients G_k, is beyond the scope of the present study and has been explored in previous works [38]. In this work, the focus is on the bifurcation induced by external inputs, deterministic (in particular periodic), stochastic, and mixed.

A. Autonomous System Analysis

The autonomous system is obtained by setting $v_s(\tau t) = 0$. It exhibits three equilibrium points, which can be identified as the intersections of the nullclines, i.e. the sets of points where $dx_1/dt = dx_2/dt = 0$, as shown in Fig. 3. The three equilibrium points are the origin, $\boldsymbol{x}_0^* = (0, 0)$, and the two points, $\boldsymbol{x}_1^* = (0.7151, -0.7151)$ and $\boldsymbol{x}_2^* = (-0.8545, 0.8545)$.

The local stability of each equilibrium point is determined from the eigenvalues of the Jacobian matrix evaluated at those points.

$$\boldsymbol{J}(x_1, x_2) = \begin{bmatrix} -1 & -1 \\ 1 & -\rho - f'(x_2) \end{bmatrix} \tag{5}$$

The equilibrium $\boldsymbol{x}_0^*$ is an unstable saddle point, characterized by one positive and one negative real eigenvalue. In contrast, $\boldsymbol{x}_1^*$ and $\boldsymbol{x}2^*$ are asymptotically stable, with complex conjugate eigenvalues having negative real parts. The basins of attraction of these two stable equilibrium points are separated by the separatrix, corresponding to the stable manifold $W^s_{\boldsymbol{x}_0^*}$ of the saddle point, shown as the blue curve in Fig. 4.

IV. Influence of a Periodic Stimulus

Periodic forcing is a common mechanism influencing neuronal dynamics. In the brain, it occurs when neuronal networks

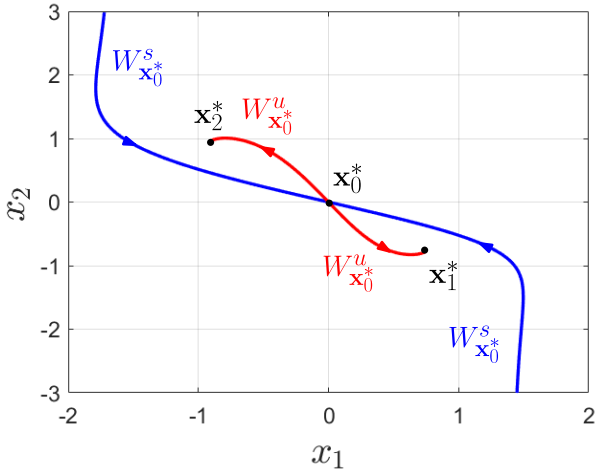

Fig. 4. Equilibrium points and their stable/unstable manifolds for the autonomous circuit. Red lines are the unstable manifold $W^u_{\boldsymbol{x}_0^*}$ of the saddle equilibrium $\boldsymbol{x}_0^*$, while blue lines are the stable manifold $W^s_{\boldsymbol{x}_0^*}$, which forms the separatrix between the basins of attraction of the two asymptotically stable equilibrium points.

are driven by inputs that follow a regular rhythmic pattern [39]. Such inputs may arise from external sensory stimulation, such as flashing lights or auditory tones [40], or from internally generated oscillatory activity in brain regions such as the thalamus during cognitive tasks [41]. These rhythmic inputs can induce neural entrainment, whereby brain oscillations synchronize with the forcing frequency, a phenomenon known as mode-locking.

We now consider the system described by Eq. (4) under the influence of a periodic external stimulus,

$$v_s(\tau t) = A \cos\left(\frac{\omega}{\omega_0} t\right), \tag{6}$$

where $\omega_0 = 1/\tau = 1/(RC)$ is the normalization frequency, and A and ω denote the amplitude and angular frequency of the stimulus, respectively.

When driven by this periodic input, the second-order system in Eq. (4) can be rewritten as the third-order autonomous system:

$$\frac{dx_1}{dt} = -(x_1 + x_2) + A\cos(x_3), \tag{7a}$$

$$\frac{dx_2}{dt} = x_1 - \rho x_2 - f(x_2), \tag{7b}$$

$$\frac{dx_3}{dt} = \frac{\omega}{\omega_0}, \tag{7c}$$

which reveals that the forced system has no equilibrium points.

We have performed extensive time domain numerical simulations to assess the system dynamic behavior. For small stimulus amplitudes, the system exhibits two asymptotically stable limit cycles, each surrounding one of the stable equilibrium points identified in the autonomous case. As the amplitude increases, the oscillations grow in magnitude and the limit cycles expand, as illustrated in Fig. 5 (a) and (b).

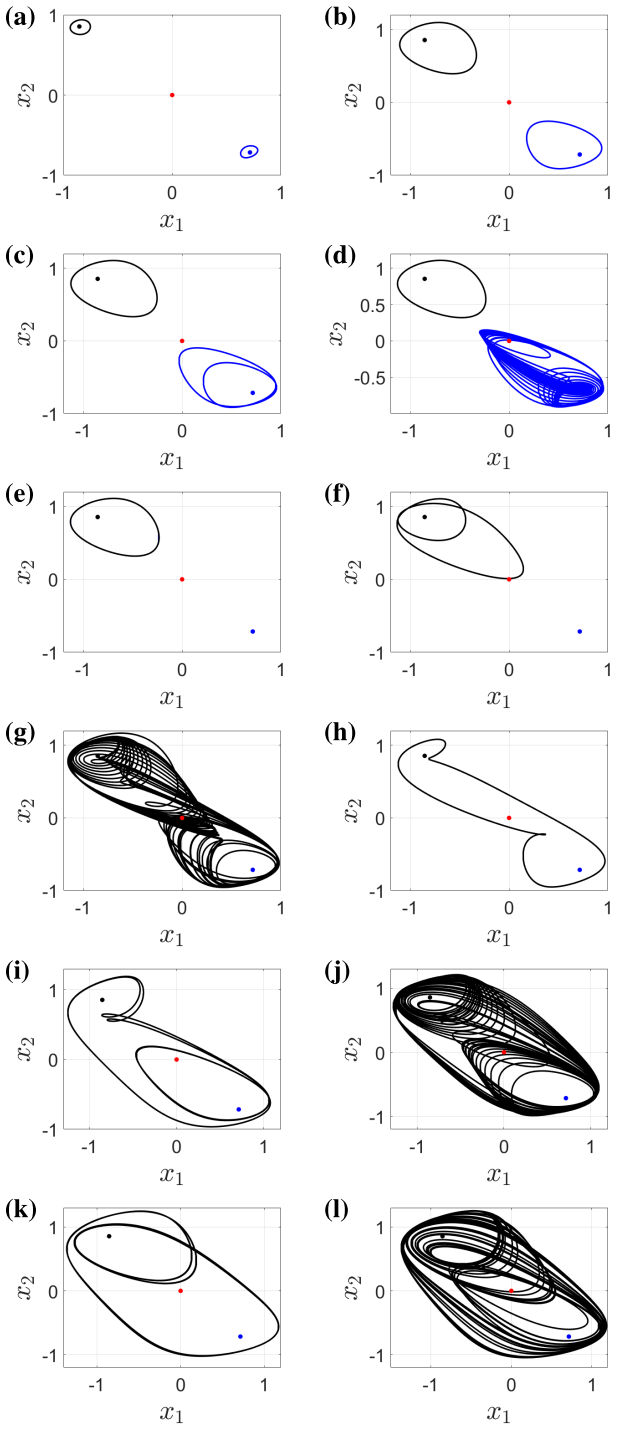

Fig. 5. Snapshots of the phase portrait for different values of the forcing amplitude A, and fixed frequency $\omega/\omega_0 = 1$. Detailed explanation is in the text. The colored dots are the equilibrium points of the autonomous system, shown here for reference. (a) Small amplitude limit cycles, $A = 0.1$. (b) The limit cycles with larger amplitude, $A = 0.32$. (c) After the period doubling (PD) bifurcation for the right cycle, $A = 0.344$. (d) After the PD cascade for the right cycle, $A = 0.34924$. (e) After the boundary crisis (BC) for the right strange attractor, $A = 0.350$. (f) After the PD bifurcation for the left limit cycle, $A = 0.381$. (g) After the PD cascade for the left limit cycle, $A = 0.3837$. (h) After the BC for the left strange attractor, $A = 0.3850$. (i) After the PD bifurcation for the large cycle, $A = 0.5844$. (j) After PD cascade for the large cycle, $A = 0.5855$. (k) After PD bifurcation for the large cycle, $A = 0.7289$. (l) After PD cascade for the large cycle, $A = 0.7350$.

When A exceeds a critical value, the right limit cycle undergoes a period-doubling bifurcation (Fig. 5 (c)), followed by a cascade of successive period doublings that culminate in the formation of a strange attractor (Fig. 5 (d)).

As the amplitude increases further, a boundary crisis occurs: the strange attractor collides with an unstable limit set, after which the attractor vanishes, leaving the left limit cycle as the unique global attractor (Fig. 5 (e)).

A similar scenario occurs for the left limit cycle. With increasing A, the limit cycle undergoes a period-doubling cascade (Fig. 5 (f)), eventually developing into a strange attractor (Fig. 5 (g)). Following another boundary crisis, this attractor disappears, giving rise to a new asymptotically stable large limit cycle (Fig. 5 (h)).

This large limit cycle then undergoes another period-doubling cascade, giving rise to a new strange attractor. A repeating pattern of boundary crises and period doublings is thus observed, alternately generating limit cycles and strange attractors as A increases (Figs. 5 (i)- 5 (l)).

A. Lyapunov Exponents

To locate and characterize the bifurcations in the parameter space, in particular transitions to chaos and boundary crises, we computed the Lyapunov's exponents.[2]

Given a continuous time dynamical system in an n-dimensional phase space, the Lyapunov exponents characterize the long-term evolution of an infinitesimal n- dimensional sphere of initial conditions. Under the flow, this sphere deforms into an n-dimensional ellipsoid due to local stretching and contraction. The Lyapunov exponents quantify the average exponential rates of divergence or convergence along the principal axes of this ellipsoid, thereby measuring the expanding or contracting nature of different directions in the phase space.

A non-autonomous dynamical system such as system (4), possesses at least one zero Lyapunov exponent, corresponding to the neutral direction tangent to the flow that reflects the time invariance of time shifted periodic solution. Directions that are, on average, expanding (contracting) correspond to positive (negative) exponents. The sum of all Lyapunov exponents equals the time-averaged divergence of the phase-space velocity. Consequently, any dissipative dynamical system must have at least one negative exponent, with the total sum being negative; thus, after transients die out, trajectories evolve on a zero-volume limit set, or *attractor*. The presence of a positive Lyapunov exponent signifies exponential sensitivity to initial conditions, a benchmark of chaotic dynamics. However, sustained exponential divergence within a bounded attractor necessitates a folding mechanism that repeatedly merges diverging trajectories, ensuring boundedness of motion. Each positive exponent therefore corresponds to a direction in which the system experiences the recurrent stretching and folding that progressively decorrelates nearby states on the attractor.

The signs of the Lyapunov exponents provide a qualitative classification of the system's long-term behavior. For a three-

[2]Readers familiar with the concept of the Lyapunov exponent can skip the following discussion and proceed directly to the description of Fig. 6.

dimensional continuous time dissipative system, the possible Lyapunov spectra and their corresponding attractors are:

$$\begin{cases} (-,-,-), & \text{fixed point (steady state)},\\ (0,-,-), & \text{limit cycle (periodic motion)},\\ (0,0,-), & \text{two-torus (quasiperiodic motion)},\\ (+,0,-), & \text{strange attractor (chaotic motion)}. \end{cases}$$

The Lyapunov exponents also provide fundamental information about information processing capabilities of the system. The regime near the transition from order to chaos, characterized by a largest nonzero Lyapunov exponent λ_m approaching zero, is often referred to as the *edge of chaos* [42], [43]. At this boundary, the system maintains a delicate balance between stability and instability: trajectories neither converge too rapidly to fixed points nor diverge uncontrollably, allowing for long-lasting, structured yet adaptable dynamics.

This regime has been extensively studied in the context of neural computation and complex systems theory. In both biological and artificial neural networks, operating near the edge of chaos has been associated with enhanced computational capabilities, including improved memory retention, sensitivity to inputs, and representational richness [44], [45], [46], [47].

For example, in reservoir computing models, maximal information transmission and learning performance occur when λ_m is close to zero, indicating that the system is neither frozen nor fully chaotic. In this critical region, perturbations are neither damped out nor amplified exponentially, allowing information to propagate and interact over extended timescales [48], [49].

It is worth noting that the beneficial role of the edge of chaos for the computational properties of reservoir computers is not universally accepted. In [50], the author notes that, in numerous reservoir computing architectures, a positive Lyapunov exponent is associated with trajectories diverging to infinity rather than with true strange attractors, a condition he termed the *edge of stability*. This distinction highlights a potential advantage of using real chaotic circuits, which operate at the true edge of chaos rather than at the edge of stability, as the basic elements of the reservoir.

In the context of the nonlinear circuit under investigation, the alternating sequence of limit cycles and strange attractors observed in Fig. 5 can be viewed as recurrent transitions across the edge-of-chaos boundary. When $\lambda_m < 0$, the system exhibits ordered, periodic behavior with high predictability but limited responsiveness to external stimuli. On the contrary, when $\lambda_m > 0$, the system becomes chaotic, exhibiting strong sensitivity to initial conditions and reduced coherence. The near-critical regime, where $\lambda_m \approx 0$, represents a dynamic balance between these extremes, allowing the system to maintain stability while exhibiting rich, high-dimensional temporal patterns. Such behavior may play an important role in adaptive or computational functions, where responsiveness and structure must coexist within the same dynamical system.

The Lyapunov exponents of system (7) are computed numerically using the standard algorithm proposed by Benettin et al. [51]. This method simultaneously integrates the original system and a set of linearized variational equations that describe the evolution of infinitesimal perturbations in phase space. Let $\dot{\boldsymbol{x}} = \boldsymbol{F}(\boldsymbol{x})$ denote the nonlinear system, and let $\delta\boldsymbol{x}$ be an infinitesimal perturbation vector. The time evolution of $\delta\boldsymbol{x}$ is governed by the variational equation

$$\dot{\delta\boldsymbol{x}} = \boldsymbol{J}(\boldsymbol{x})\,\delta\boldsymbol{x}, \tag{8}$$

where $\boldsymbol{J}(\boldsymbol{x}) = \partial\boldsymbol{F}/\partial\boldsymbol{x}$ is the Jacobian matrix evaluated along the trajectory $\boldsymbol{x}(t)$ of the system. To compute the full spectrum of Lyapunov exponents, an orthonormal basis of n perturbation vectors $\{\boldsymbol{v}_1, \boldsymbol{v}_2, \ldots, \boldsymbol{v}_n\}$ is evolved according to Eq. (8). At regular time intervals Δt_r, the perturbation vectors are orthonormalized using the Gram–Schmidt procedure, and the logarithms of the stretching factors are accumulated. After a sufficiently long integration time T, the Lyapunov exponents are estimated as

$$\lambda_i = \frac{1}{T}\sum_{k=1}^{N} \ln \frac{\|\boldsymbol{v}_i^{(k)}\|}{\|\boldsymbol{v}_i^{(k-1)}\|}, \qquad i = 1, 2, \ldots, n, \tag{9}$$

where $N = T/\Delta t_r$ is the total number of renormalization steps. In the present work, the system equations and their corresponding variational equations are integrated using a fourth-order Runge–Kutta method with a fixed time step $\Delta t = 10^{-3}$ (dimensionless unit). The integration time is chosen sufficiently long to ensure convergence of the Lyapunov exponents to their asymptotic values. To identify transitions between periodic, quasiperiodic, and chaotic regimes, the largest Lyapunov exponent λ_m (beside the "structural" one which is always equal to zero) is monitored as a function of the control parameters A and ω. A positive value of λ_m indicates chaos, while $\lambda_m = 0$ and $\lambda_m < 0$ correspond to quasiperiodic and periodic motion, respectively.

Fig. 6 (a) shows the bifurcation diagram (Poincaré map) of the system in (7). The values of $x_2(t_k)$ are plotted as a function of the forcing amplitude A, with $\omega/\omega_0 = 1$. Here, $t_k = t_0 + \frac{2\pi k}{\omega}$, where $k = 1, 2, \ldots$, and t_0 denotes the time at which $x_2(t)$ attains its first maximum (after the transient has decayed).[3] The chaotic regions (vertical bands with densely distributed points) and the periodic windows can be clearly identified.

Fig. 6 (b) presents λ_m as a function of the stimulus amplitude in the range $0.3 < A < 1.2$, for $\omega/\omega_0 = 1$. In this region of the parameter space, the system exhibits a unique global attractor. The behavior of λ_m clearly reveals alternating transitions between periodic dynamics, corresponding to $\lambda_m < 0$, and chaotic dynamics, associated with a strange attractor for which $\lambda_m > 0$.

Fig. 7 shows the main bifurcation curves in the parameter space (A, ω) for system (7). The bifurcation curves were obtained using a numerical continuation method to track the relevant solution branches in parameter space. In particular, periodic solutions (limit cycles) were computed using a shooting technique, whereby periodic orbits are formulated as fixed points of the flow over one forcing period and solved iteratively. To robustly follow these solutions as parameters vary, including near turning points, pseudo–arclength continuation was employed, enabling continuation along solution branches

[3] This periodic sampling of the system's state every one period is sometime referred to as a "stroboscopic map".

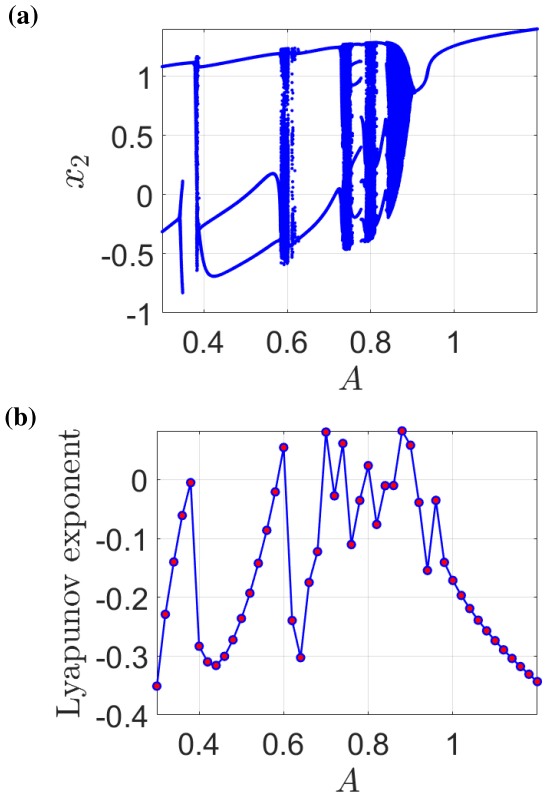

Fig. 6. (a) Poincaré map of the system in (7) showing the values of $x_2(t_k)$ as a function of the forcing amplitude A, with $\omega/\omega_0 = 1$. The section is defined by $t_k = t_0 + \frac{2\pi k}{\omega}$, where t_0 denotes the time at which $x_2(t)$ attains its first maximum (after the transient has decayed). The diagram illustrates the evolution of the system dynamics as A increases, highlighting periodic windows and chaotic (multi-valued) regions. (b) Largest non-null Lyapunov exponent λ_m with $\omega/\omega_0 = 1$. For $A < 0.35$ only the Lyapunov exponent for the left limit cycle is shown. The regions with positive λ_m correspond to the chaotic regions in Fig. 6(a). Note that λ_m becomes slightly positive in a small interval around $A \simeq 0.383$. This interval corresponds to the strange attractor shown in Fig. 5(g).

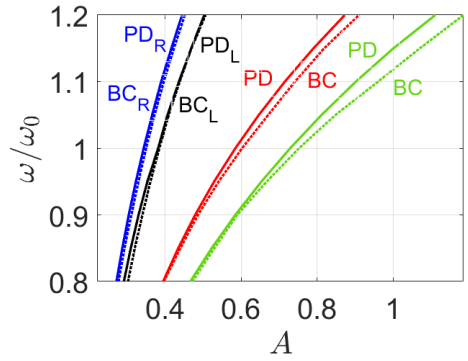

Fig. 7. Bifurcation structure of system (7) in the parameter space (A, ω). Solid lines denote the first period-doubling bifurcations in the respective period-doubling cascades, while dashed lines correspond to boundary-crisis curves. The curves labeled PD_R and BC_R refer to the small limit cycle surrounding the equilibrium point $\boldsymbol{x}_1^*$. PD_L and BC_L correspond to the small limit cycle surrounding $\boldsymbol{x}_2^*$. The red and green curves, labeled PD and BC, indicate the first and second period-doubling cascades and the associated boundary crisis for the large limit cycle and the corresponding strange attractor, respectively.

independently of a single parameter [52]. Period-doubling bifurcations were detected by monitoring changes in the period of the computed limit cycles.

In regimes where the dynamics evolved toward strange attractors, the analysis was complemented by the computation of Lyapunov exponents, which allowed us to characterize the onset of chaos and the stability properties of the resulting attractors. The bifurcation analysis was further supported by the study of the Poincaré map shown in Fig. 6 (a).

Solid lines denote the first period-doubling bifurcation in each period-doubling cascade, while dashed lines correspond to boundary crisis curves. The curves labeled PD_R and BC_R refer to the period-doubling and boundary-crisis transitions of the small limit cycle surrounding the equilibrium point $\boldsymbol{x}_1^*$ of the autonomous system. PD_L and BC_L correspond to the analogous transitions for the left limit cycle surrounding $\boldsymbol{x}_2^*$. The red and green curves, labeled PD and BC, represent the first and second period-doubling cascades and the associated boundary crises of the large limit cycle and the resulting strange attractor, respectively.

It is worth noting that the strange attractors occur only within relatively narrow intervals of parameter values. From a computational perspective, this feature is advantageous. Optimal information processing is typically associated with operation at the edge of chaos, namely in parameter regions that border chaotic regimes but do not correspond to fully developed chaos. In fully chaotic states, the dynamics become highly unpredictable, entropy production is maximal, and information is rapidly degraded. The presence of several small chaotic regions in parameter space therefore provides multiple edge-of-chaos operating regimes, which may enhance the flexibility and computational potential of the system.

V. Effect of Stochastic Perturbations and Noise-Induced Dynamics

We now extend our analysis by considering the case in which the external periodic stimulus incorporates a random component, modeled as an additive white Gaussian noise.

Real-world systems are inevitably subject to disturbances. In complex environments, where a sufficiently large number of independent sources contribute to the perturbations, the resulting fluctuations are Gaussian distributed, as established by the central limit theorem. When the energy of these disturbances is distributed over a wide frequency range, white Gaussian noise provides an appropriate model for their effect. In our study, the external perturbations, both deterministic and stochastic, represent stimuli applied to the circuit. The stochastic component, in particular, models background noise, which may be applied either independently or together with the deterministic signal.

The input signal is assumed to be of the form:

$$v_s(t) = g(t) + D\frac{dW(t)}{dt}, \tag{10}$$

where D represents the intensity of the stochastic perturbation and $W(t)$ is a Wiener process characterized by zero initial value $W(0) = 0$, zero mean $\mathrm{E}[W(t)] = 0$, and variance $\mathrm{var}[W(t)] = t$. Under this assumption, the system (2) becomes a set of stochastic differential equations (SDEs). Because the amplitude of the noise is constant (commonly referred to as unmodulated or additive noise) the solutions are identical

under both the Itô's and the Stratonovich's interpretation of SDEs [53]. We emphasize that the random term should be interpreted as an external perturbation, because modeling internal noise in nonlinear dissipative elements as Gaussian white noise with constant intensity leads to violations of the fundamental laws of thermodynamics [54], [55].

Under rescaling of the time variable $t = \tau t'$, the Wiener process transforms according to [56] and [57]

$$W(t') \sim \sqrt{\frac{1}{\tau}}\, W(t), \tag{11}$$

where "$\sim$" denotes equality in distribution. Consequently, the rescaled system converges in probability to the solution of the SDEs:

$$\frac{dx_1}{dt} = -\big(x_1 + x_2\big) + g(t) + \varepsilon\, \frac{dW(t)}{dt}, \tag{12a}$$

$$\frac{dx_2}{dt} = x_1 - \rho x_2 - f(x_2), \tag{12b}$$

where the dimensionless noise intensity is $\varepsilon = DR\sqrt{RC}/L$, and as before, we have written t instead of t' for notational simplicity.

It is convenient to introduce new variables,

$$x = x_2 \tag{13a}$$

$$y = x_1 - \rho\, x_2 - f(x_2) \tag{13b}$$

which transform system (12) into the SDEs

$$\frac{dx}{dt} = y \tag{14a}$$

$$\frac{dy}{dt} = -U'(x) - U''(x)\, y + g(t) + \varepsilon \frac{dW(t)}{dt} \tag{14b}$$

where

$$U(x) = \int [(1+\rho)x + f(x)]\, dx \tag{15}$$

is the effective potential.

The SDEs (14) describe the Brownian motion of a particle in the potential landscape $U(x)$, subject to the nonlinear friction $F(x, y) = U''(x)\, y$ and the force $g(t)$.

Asymptotically stable (respectively, unstable) equilibrium points of the autonomous system, that is, for $g(t) = 0$ and $\varepsilon = 0$, correspond to values of x located at the local minima (respectively, maxima) of the effective potential $U(x)$, with $y = 0$. The position of the equilibrium points and the stable/unstable manifolds of the saddle for the system in the new coordinates are shown in Fig. 8.

The influence of noise on the system's dynamic behavior was investigated through numerical simulations. The SDEs (14) were solved using a stochastic Runge–Kutta integration scheme with strong order-one convergence [58]. A fixed time step of $\delta t = 10^{-4}$ was employed, and each simulation was run for a total duration of $\Delta T = 10^3$ (dimensionless units) to ensure statistical convergence of the results. The stochastic term was modeled as additive Gaussian white noise with zero mean and variance proportional to δt. Random numbers were generated using the ziggurat method [59].

In selecting the noise intensity, we assume that the stochastic term represents background noise, either intrinsically present or superimposed on the periodic signal that models the external stimulus. Accordingly, the noise amplitude is chosen to be from one to three orders of magnitude smaller than that of the periodic signal, so that it acts as a perturbative contribution rather than as a dominant driving mechanism. In fact, the relevant parameter is the ratio between the amplitude of the periodic forcing and the noise intensity, which determines the effective signal-to-noise balance of the system.

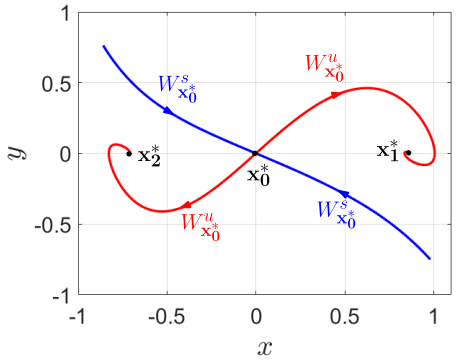

Fig. 8. Equilibrium points and their stable/unstable manifolds for the system in the new variables. Red lines denote the unstable manifold $W^u_{\boldsymbol{x}_0^*}$ of the saddle equilibrium $\boldsymbol{x}_0^*$, while blue lines denote the stable manifold $W^s_{\boldsymbol{x}_0^*}$, which forms the separatrix between the basins of attraction of the two asymptotically stable equilibrium points.

In the absence of external forcing and for small noise intensities, the particle remains confined within one of the potential wells. Starting from random initial conditions, it is attracted toward one of the asymptotically stable equilibrium points, which one depends on the initial condition, and converges to it along the corresponding stable manifold. Subsequently, the particle exhibits small fluctuations around this stable equilibrium point (see Fig. 9 (a) and (b)). Notably, since the variance of the Wiener process increases linearly in time, the particle will escape the potential well with probability one given sufficient long time.

As the noise intensity increases, the particle may acquire sufficient kinetic energy to overcome the potential barrier separating adjacent wells of the effective potential $U(x)$ in a finite time. When the stochastic fluctuations become comparable to the barrier height, random transitions between neighboring potential wells can occur. These *noise-induced transitions* illustrate the system's ability to switch between coexisting stable states under the influence of random perturbations. This behavior is exemplified in Fig. 9 (c) and (d). Starting from random initial conditions, the particle initially converges toward a stable equilibrium point along its stable manifold and subsequently fluctuates around it. At a random instant, a sufficiently strong noise-induced fluctuation enables the particle to cross the separatrix, leading it to transition to the other equilibrium point.

As the noise intensity increases further, the particle's kinetic energy correspondingly rises, leading to larger fluctuation amplitudes. Transitions between adjacent potential wells become more frequent, and the temporal evolution of the system begins to display characteristics of noise-induced

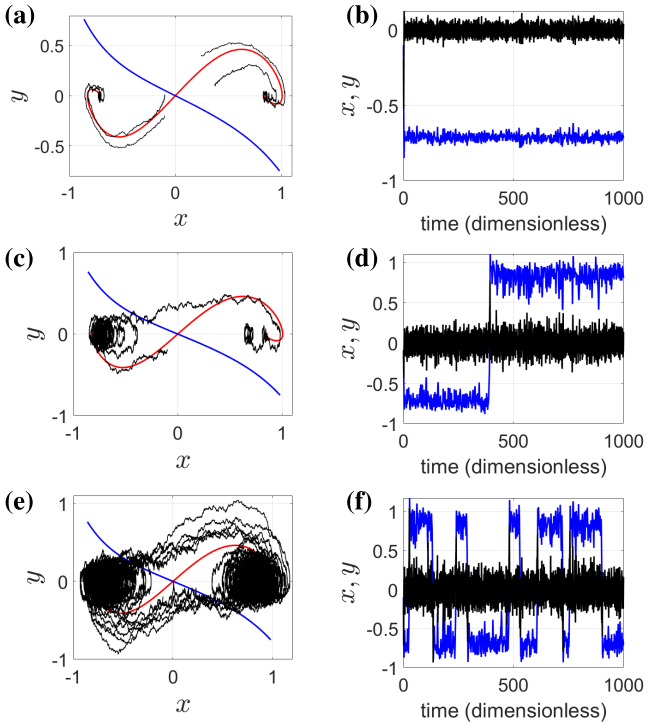

Fig. 9. Trajectories in the state space (figures (a), (c) and (e), black lines) and the time evolution (figures (b), (d) and (f)) representing the solution of the SDEs (14) for random initial conditions and different realization of the Wiener process. The stable and unstable manifolds of the saddle equilibrium point for the autonomous system are shown for reference. (a) Four trajectories starting from distinct random initial conditions, noise intensity is $D = 10^{-3}$. (b) The corresponding time evolution of one of these solutions. (c) State space trajectory for $D = 3 \cdot 10^{-3}$, and (d) the corresponding time evolution. (e) State space trajectory for $D = 4 \cdot 10^{-3}$ and (f) the corresponding time evolution.

oscillatory dynamics between the coexisting stable states (Fig. 9 (e) and (f)).

The mean oscillation frequency can be estimated, at least approximately, by the Eyring-Kramers formula [60]. Given the SDEs

$$\frac{dx}{dt} = y \tag{16a}$$

$$\frac{dy}{dt} = -U'(x) - \gamma y + \varepsilon \frac{dW(t)}{dt} \tag{16b}$$

where γ is a damping coefficient, the Eyring-Kramers formula for the average transition time between the state x_i^* and the state x_j^* through the unstable saddle x_0^* is:

$$\mathrm{E}[\tau_{x_i^* \to x_j^*}] = \frac{4\pi}{\sqrt{\gamma^2 - 4U''(x_0^*)} - \gamma} \sqrt{\frac{|U''(x_0^*)|}{U''(x_i^*)}} \times \exp\left(\frac{2\gamma \Delta U(x_0^*, x_i^*)}{\varepsilon^2}\right) \tag{17}$$

where $\Delta U(x_0^*, x_i^*) = U(x_0^*) - U(x_i^*)$ is the height of the potential barrier.

To the best of the authors' knowledge, there is no extension of the Eyring–Kramers formula applicable to systems with nonlinear friction. Therefore, we linearize the friction term in Eq. (14) by setting $\gamma = U''(x_0^*)$, and subsequently apply Eq. (17). Fig. 10 presents a comparison between the expected

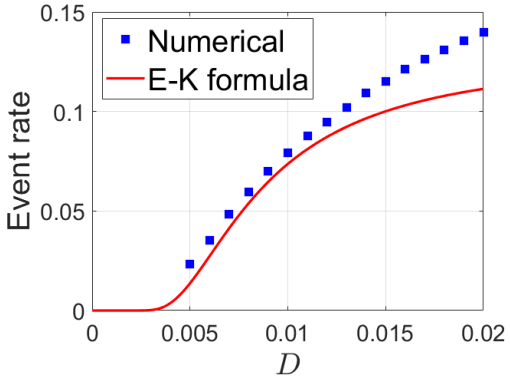

Fig. 10. Event rate (number of transitions between the basins of attraction of the stable equilibrium points per unit time), for system (14) with $g(t) = 0$. Comparison between numerical simulations and theoretical prediction from the Eyring-Kramers formula (17).

transition time as a function of noise intensity obtained from the Eyring–Kramers formula and that computed from numerical simulations.

The Eyring–Kramers formula is classically derived for systems with linear damping evolving in a multi-well potential, where metastability is determined by the presence of multiple minima in the potential landscape. In the present circuit, however, multistability does not originate from a multi-well potential but from the nonlinear friction induced by the nonvolatile memristor.

Using the change of coordinates introduced in (13), the dynamics can be reformulated in terms of an effective higher-order potential exhibiting multiple minima. This representation establishes a formal correspondence between friction-induced and potential-induced multistability, thereby providing a theoretical basis for applying the Eyring–Kramers approximation to our system. Comparison with numerical results (see Fig. 10) confirms the validity of this approach, showing good agreement even for moderately large noise intensities, with the expected degradation as the noise strength increases.

To evaluate the mean oscillation frequency of the noise-induced oscillations, we define an event as the particle crossing the separatrix between the two potential wells.[4] The noise-induced oscillation frequency is therefore defined as half the number of such events, normalized by the total simulation time. The mean oscillation frequency was estimated from numerical simulations performed using the integration step and total duration specified above. To ensure robust estimates, we conducted 100 simulations for each noise intensity; in each simulation, the initial transient (the first 50 s) was discarded, and the event rate was computed by averaging over all realizations. As expected, the Eyring-Kramers formula offers accurate prediction for small noise intensities.

A. Stochastic Resonance

To conclude the analysis, we investigate the interplay between a random and a periodic excitation, which gives rise

[4]It is important to consider the crossing of the barrier rather than merely reaching it, since a particle that only reaches the barrier has a one-half probability of being reflected back into the initial potential well.

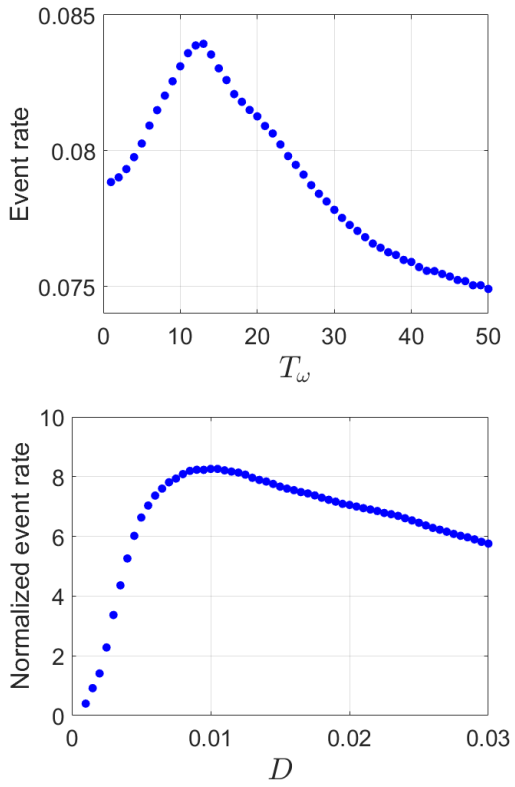

Fig. 11. Event rate (number of transitions between the basins of attraction of the stable equilibrium points per unit time), for system (14) with $g(t) = A\cos(\omega t)$. Top: Event rate as a function of the forcing period T_ω, for $D = 10^{-}2$ (dimensionless unit). Bottom: Normalized event rate (event rate divided by the noise intensity) as a function of D, for $T_\omega = 14$ (dimensionless units).

to the phenomenon of *stochastic resonance* [61]. In bistable systems, the mechanism underlying stochastic resonance is straightforward. In the presence of a periodic forcing of the form $g(t) = A\cos(\omega t)$, the double-well potential is periodically tilted, alternately raising and lowering the potential barrier. At time instants $t = k\pi/\omega$, the circuit dynamics is equivalent to the motion of a Brownian particle in an "effective" potential $V(x) = U(x) + A\,x$, with the right well raised and the left well lowered. Half a period later, at $t = (2k+1)\pi/\omega$, the situation is reversed. Although the noise intensity alone may be insufficient to induce barrier crossing, the combination of fluctuations and the periodic raising/lowering of the barrier height can lead to synchronized jumps between the potential wells.

To achieve statistical synchronization, the average transition time between two noise-induced interwell transitions must be comparable with half the period of the forcing, yielding the matching condition for stochastic resonance:

$$T_\omega = \frac{2\pi}{\omega} = \mathrm{E}[\tau_{x_1^*\to x_2^*}] + \mathrm{E}[\tau_{x_2^*\to x_1^*}] \tag{18}$$

Numerical simulations confirm that stochastic resonance occurs in the proposed circuit, in agreement with classical theory. Fig. 11 illustrates two typical characterizations of this phenomenon. In the top panel, the event rate is shown as a function of the period of the forcing signal for a fixed noise intensity $D = 10^{-2}$ (dimensionless units). The curve exhibits a pronounced peak at the frequency corresponding to $T_\omega \approx 14$, which is very close to twice the average exit time $\mathrm{E}[\tau_{x_1^*\to x_2^*}] + \mathrm{E}[\tau_{x_2^*\to x_1^*}] = 13.58$ predicted by the Eyring–Kramers formula. In the bottom panel, the normalized event rate (i.e., the number of events per unit time, normalized to the noise intensity and analogous to a signal-to-noise ratio) is plotted as a function of the noise intensity D for a fixed forcing period $T_\omega = 14$ (dimensionless units). Once again, the curve displays a clear maximum at $D = 0.01$, the noise intensity for which the mean exit time matches half the forcing period. Numerical simulations were performed using the setup described above. For clearer visualization and to obtain a smoother curves, the data were smoothed using a 5-point moving average, with each value computed over a sliding window of length 5 (truncated at the endpoints) applied to neighboring elements of the event-rate vector. The smoothing operation does not shift the peak location in the plots.

VI. Conclusion

We have presented a comprehensive investigation of multistability, noise-induced transitions, and stochastic resonance in a second-order nonlinear oscillator incorporating an experimentally characterized nonvolatile memristive device. The memristor-based circuit provides a compact, physically realizable platform for studying complex nonlinear dynamics and stochastic phenomena relevant to neuromorphic computing and brain-inspired artificial intelligence systems.

The autonomous system exhibits bistable behavior with two asymptotically stable equilibrium points separated by a saddle point, whose stable manifold forms the separatrix between their respective basins of attraction. Under periodic excitation, the system displays rich dynamical behavior including coexisting limit cycles, period-doubling cascades, boundary crises, and transitions to chaos. Lyapunov exponent analysis revealed that the system repeatedly crosses the edge-of-chaos regime, a critical dynamical state where the largest nonzero Lyapunov exponent approaches zero. This regime represents a delicate balance between stability and sensitivity to perturbations, and has been associated with enhanced computational capabilities in both biological and artificial neural networks, including improved memory retention, information transmission, and representational richness.

The effects of additive Gaussian white noise have been analyzed by reformulating the system dynamics in terms of an effective potential landscape. In this framework, noise induces random transitions between coexisting attractors, with the circuit behaving like a particle executing Brownian motion in a double-well potential subject to nonlinear friction. For weak noise intensities, transition rates are accurately predicted by the Eyring-Kramers formula, which captures the exponential dependence of escape times on the ratio of barrier height to noise intensity. As noise intensity increases, the system exhibits noise-induced oscillations with a characteristic frequency determined by the average inter-well transition time.

When periodic forcing and noise act jointly, the system exhibits stochastic resonance, a counterintuitive phenomenon in which the presence of noise enhances the system's response to weak periodic signals. Optimal synchronization occurs

when the forcing period matches twice the mean noise-induced transition time, satisfying the classical matching condition for stochastic resonance. Numerical simulations confirm this behavior, with pronounced peaks in the event rate observed at the predicted resonance conditions.

These results demonstrate that memristor-based nonlinear circuits naturally operate near critical dynamical regimes and provide a compact hardware platform for implementing neuromorphic functions that exploit noise-assisted computation. The programmable nonlinearity offered by the nonvolatile memristor enables tuning of the potential landscape, basin boundaries, and bifurcation structure, suggesting applications in adaptive systems requiring reconfigurable multistable dynamics. The edge-of-chaos operation identified in this work is particularly relevant for reservoir computing and echo state networks, where computational performance is maximized in critical regimes exhibiting both stability and sensitivity.

These results provide a foundation for developing learning algorithms that leverage multistability and stochastic resonance in memristor-based nonlinear oscillators, offering a promising route toward energy-efficient, brain-inspired computing platforms capable of real-time adaptation and robust decision-making under uncertainty.

ACKNOWLEDGMENT

This manuscript reflects only the authors' views and opinions, neither the European Union nor the European Commission can be considered responsible for them.

REFERENCES

[1] X.-J. Wang, "Decision making in recurrent neuronal circuits," *Neuron*, vol. 60, no. 2, pp. 215–234, Oct. 2008.

[2] D. Durstewitz, N. M. Vittoz, S. B. Floresco, and J. K. Seamans, "Abrupt transitions between prefrontal neural ensemble states accompany behavioral transitions during rule learning," *Neuron*, vol. 66, no. 3, pp. 438–448, May 2010.

[3] A. Ponce-Alvarez, V. Nácher, R. Luna, A. Riehle, and R. Romo, "Dynamics of cortical neuronal ensembles transit from decision making to storage for later report," *J. Neurosci.*, vol. 32, no. 35, pp. 11956–11969, Aug. 2012.

[4] K. W. Latimer, J. L. Yates, M. L. R. Meister, A. C. Huk, and J. W. Pillow, "Single-trial spike trains in parietal cortex reveal discrete steps during decision-making," *Science*, vol. 349, no. 6244, pp. 184–187, Jul. 2015.

[5] P. Miller and D. B. Katz, "Stochastic transitions between neural states in taste processing and decision-making," *J. Neurosci.*, vol. 30, no. 7, pp. 2559–2570, Feb. 2010.

[6] Y. Burak and I. R. Fiete, "Accurate path integration in continuous attractor network models of grid cells," *PLoS Comput. Biol.*, vol. 5, no. 2, Feb. 2009, Art. no. e1000291.

[7] X. Zhang, X. Long, S.-J. Zhang, and Z. S. Chen, "Excitatory-inhibitory recurrent dynamics produce robust visual grids and stable attractors," *Cell Rep.*, vol. 41, no. 11, Dec. 2022, Art. no. 111777.

[8] E. Curti, G. Mongillo, G. L. Camera, and D. J. Amit, "Mean field and capacity in realistic networks of spiking neurons storing sparsely coded random memories," *Neural Comput.*, vol. 16, no. 12, pp. 2597–2637, Dec. 2004.

[9] I. Gat, N. Tishby, and M. Abeles, "Hidden Markov modelling of simultaneously recorded cells in the associative cortex of behaving monkeys," *Network: Comput. Neural Syst.*, vol. 8, no. 3, pp. 297–322, Aug. 1997.

[10] L. M. Jones, A. Fontanini, B. F. Sadacca, P. Miller, and D. B. Katz, "Natural stimuli evoke dynamic sequences of states in sensory cortical ensembles," *Proc. Nat. Acad. Sci. USA*, vol. 104, no. 47, pp. 18772–18777, Nov. 2007.

[11] B. F. Sadacca, N. Mukherjee, T. Vladusich, J. X. Li, D. B. Katz, and P. Miller, "The behavioral relevance of cortical neural ensemble responses emerges suddenly," *J. Neurosci.*, vol. 36, no. 3, pp. 655–669, Jan. 2016.

[12] J. J. Hopfield, "Neural networks and physical systems with emergent collective computational abilities," *Proc. Nat. Acad. Sci. USA*, vol. 79, no. 8, pp. 2554–2558, 1982.

[13] H. Y. Chan and S. H. Zak, "On neural networks that design neural associative memories," *IEEE Trans. Neural Netw.*, vol. 8, no. 2, pp. 360–372, Mar. 1997.

[14] W. Lin and G. Chen, "Large memory capacity in chaotic artificial neural networks: A view of the anti-integrable limit," *IEEE Trans. Neural Netw.*, vol. 20, no. 8, pp. 1340–1351, Aug. 2009.

[15] H. Deng, G. Stathopoulos, and C. Y. Suen, "Applying error-correcting output coding to enhance convolutional neural network for target detection and pattern recognition," in *Proc. 20th Int. Conf. Pattern Recognit.*, Aug. 2010, pp. 4291–4294.

[16] J. Schmidhuber, "Deep learning in neural networks: An overview," *Neural Netw.*, vol. 61, pp. 85–117, Jan. 2015.

[17] R. Y. Choi, A. S. Coyner, J. Kalpathy-Cramer, M. F. Chiang, and J. P. Campbell, "Introduction to machine learning, neural networks, and deep learning," *Transl. Vis. Sci. Technol.*, vol. 9, no. 2, p. 14, 2020.

[18] K. S. Narendra and S. Mukhopadhyay, "Intelligent control using neural networks," *IEEE Control Systems Magazine*, vol. 12, no. 2, pp. 11–18, Feb. 2002.

[19] Y. Becerikli, A. F. Konar, and T. Samad, "Intelligent optimal control with dynamic neural networks," *Neural Netw.*, vol. 16, no. 2, pp. 251–259, Mar. 2003.

[20] M. Vidyasagar, "Location and stability of the high-gain equilibria of nonlinear neural networks," *IEEE Trans. Neural Netw.*, vol. 4, no. 4, pp. 660–672, Apr. 1993.

[21] M. Forti, S. Manetti, and M. Marini, "A condition for global convergence of a class of symmetric neural circuits," *IEEE Trans. Circuits Syst. I, Fundam. Theory Appl.*, vol. 39, no. 6, pp. 480–483, Jun. 2002.

[22] J. Zhang, S. Zhu, G. Bao, X. Liu, and S. Wen, "Analysis and design of multivalued high-capacity associative memories based on delayed recurrent neural networks," *IEEE Trans. Cybern.*, vol. 52, no. 12, pp. 12989–13000, Dec. 2022.

[23] W. Maass, T. Natschläger, and H. Markram, "Real-time computing without stable states: A new framework for neural computation based on perturbations," *Neural Comput.*, vol. 14, no. 11, pp. 2531–2560, Nov. 2002.

[24] V. Mante, D. Sussillo, K. V. Shenoy, and W. T. Newsome, "Context-dependent computation by recurrent dynamics in prefrontal cortex," *Nature*, vol. 503, no. 7474, pp. 78–84, Nov. 2013.

[25] D. Marković, A. Mizrahi, D. Querlioz, and J. Grollier, "Physics for neuromorphic computing," *Nature Rev. Phys.*, vol. 2, no. 9, pp. 499–510, Jul. 2020.

[26] Q. Duan et al., "Spiking neurons with spatiotemporal dynamics and gain modulation for monolithically integrated memristive neural networks," *Nature Commun.*, vol. 11, no. 1, p. 3399, Jul. 2020.

[27] Q. Shao, Z. Wang, and J. J. Yang, "Efficient AI with MRAM," *Nature Electron.*, vol. 5, no. 2, pp. 67–68, Feb. 2022.

[28] H. Cai et al., "Brain organoid reservoir computing for artificial intelligence," *Nature Electron.*, vol. 6, no. 12, pp. 1032–1039, Dec. 2023.

[29] H. Lin, C. Wang, Q. Hong, and Y. Sun, "A multi-stable memristor and its application in a neural network," *IEEE Trans. Circuits Syst. II, Exp. Briefs*, vol. 67, no. 12, pp. 3472–3476, Dec. 2020.

[30] M. Di Marco, M. Forti, and L. Pancioni, "Convergence and multistability of nonsymmetric cellular neural networks with memristors," *IEEE Trans. Cybern.*, vol. 47, no. 10, pp. 2970–2983, Oct. 2017.

[31] S. Zhang, L. Liu, C. Wang, X. Zhang, and R. Ma, "Multistability and global attractivity for fractional-order spiking neural networks," *Appl. Math. Comput.*, vol. 508, Jan. 2026, Art. no. 129617.

[32] D. B. Strukov, G. S. Snider, D. R. Stewart, and R. S. Williams, "The missing memristor found," *Nature*, vol. 453, no. 7191, pp. 80–83, May 2008.

[33] J. J. Yang, D. B. Strukov, and D. R. Stewart, "Memristive devices for computing," *Nature Nanotechnol.*, vol. 8, no. 1, pp. 13–24, 2013.

[34] Z. Li, J. Jin, D. Zhang, and C. Chen, "An attractor-controllable memristive Hopfield neural network and its application on voice encryption," *Integration*, vol. 2025, Aug. 2025, Art. no. 102500.

[35] E. Wu et al., "Universal core–shell nanowire memristor platform with quasi-2D filament confinement for scalable neuromorphic applications," *Adv. Funct. Mater.*, vol. 36, no. 11, p. 18764, Feb. 2026.

[36] S. Brivio, J. Frascaroli, and S. Spiga, "Role of metal-oxide interfaces in the multiple resistance switching regimes of Pt/HfO_2/TiN devices," *Appl. Phys. Lett.*, vol. 107, no. 2, Jul. 2015, Art. no. 023504.

[37] J. Frascaroli, F. G. Volpe, S. Brivio, and S. Spiga, "Effect of al doping on the retention behavior of HfO_2 resistive switching memories," *Microelectronic Eng.*, vol. 147, pp. 104–107, Nov. 2015.

[38] M. Escudero et al., "Chua's circuit with tunable nonlinearity based on a nonvolatile memristor: Design and realization," *IEEE Trans. Circuits Syst. I, Reg. Papers*, vol. 71, no. 1, pp. 62–72, Jan. 2024.

[39] E. M. Izhikevich, "Neural excitability, spiking and bursting," *Int. J. Bifurcation Chaos*, vol. 10, no. 6, pp. 1171–1266, Jun. 2000.
[40] A. Longtin, A. Bulsara, D. Pierson, and F. Moss, "Bistability and the dynamics of periodically forced sensory neurons," *Biol. Cybern.*, vol. 70, no. 6, pp. 569–578, Apr. 1994.
[41] M. Tsanov et al., "Oscillatory entrainment of thalamic neurons by theta rhythm in freely moving rats," *J. Neurophysiol.*, vol. 105, no. 1, pp. 4–17, 2011.
[42] J. P. Crutchfield and K. Young, "Computation at the onset of chaos," in *Complexity, Entropy, and the Physics of Information*, W. H. Zurek, Ed., Reading, MA, USA: Addison-Wesley, 1988, pp. 223–269.
[43] C. G. Langton, "Computation at the edge of chaos," *Phys. D, Nonlinear Phenomena*, vol. 42, nos. 1–3, pp. 12–37, 1990.
[44] N. Bertschinger and T. Natschläger, "Real-time computation at the edge of chaos in recurrent neural networks," *Neural Comput.*, vol. 16, no. 7, pp. 1413–1436, Jul. 2004.
[45] J. Boedecker, O. Obst, J. T. Lizier, N. M. Mayer, and M. Asada, "Information processing in echo state networks at the edge of chaos," *Theory Biosciences*, vol. 131, no. 3, pp. 205–213, Sep. 2012.
[46] A. Ascoli, A. S. Demirkol, R. Tetzlaff, and L. Chua, "Edge of chaos theory resolves Smale paradox," *IEEE Trans. Circuits Syst. I, Reg. Papers*, vol. 69, no. 3, pp. 1252–1265, Mar. 2022.
[47] A. Ascoli et al., "Edge of chaos theory unveils the first and simplest ever reported Hodgkin–Huxley neuristor," *Adv. Electron. Mater.*, vol. 11, no. 8, 2025, Art. no. 2400789.
[48] J. T. Lizier, M. Prokopenko, and A. Y. Zomaya, "The information dynamics of the edge of chaos in random Boolean networks," *Artif. Life*, vol. 17, no. 4, pp. 293–314, 2011.
[49] J. Moreno-Ribera, R. Gallego, and F. Martínez, "Chaotic dynamics optimize learning in spiking neural networks," *Phys. Rev. Lett.*, vol. 123, no. 20, 2019, Art. no. 208101.
[50] T. L. Carroll, "Do reservoir computers work best at the edge of chaos?," *Chaos, Interdiscipl. J. Nonlinear Sci.*, vol. 30, no. 12, 2020, Art. no. 121109.
[51] G. Benettin, L. Galgani, A. Giorgilli, and J.-M. Strelcyn, "Lyapunov characteristic exponents for smooth dynamical systems and for Hamiltonian systems; A method for computing all of them. Part 1: Theory; Part 2: Numerical application," *Meccanica*, vol. 15, no. 1, pp. 9–30, 1980.
[52] E. L. Allgower and K. Georg, *Introduction to Numerical Continuation Methods*. Philadelphia, PA, USA: SIAM, 2003.
[53] B. Øksendal, *Stochastic Differential Equations*. Cham, Switzerland: Springer, 2003.
[54] L. Désoppi and B. Reulet, "Link between continuous and discrete descriptions of noise in nonlinear resistive electrical components," *Fluctuation Noise Lett.*, Sep. 2025, Art. no. 2540014.
[55] M. Bonnin, F. Bonani, J.-C. Delvenne, L. Van Brandt, and F. Traversa, "Thermodynamically consistent noise modeling in non-linear circuits," *Fluctuation Noise Lett.*, Oct. 2025, Art. no. 2540019.
[56] M. Bonnin, K. Song, F. L. Traversa, and F. Bonani, "Model order reduction and stochastic averaging for the analysis and design of micro-electro-mechanical systems," *Nonlinear Dyn.*, vol. 112, no. 5, pp. 3421–3439, Mar. 2024.
[57] K. Song, M. Bonnin, F. L. Traversa, and F. Bonani, "A stochastic averaging mathematical framework for design and optimization of nonlinear energy harvesters with several electrical DOFs," *Commun. Nonlinear Sci. Numer. Simul.*, vol. 139, Dec. 2024, Art. no. 108306.
[58] S. Särkkä and A. Solin, *Applied Stochastic Differential Equations*. Cambridge, U.K.: Cambridge Univ. Press, 2019.
[59] G. Marsaglia and W. W. Tsang, "The Ziggurat method for generating random variables," *J. Stat. Softw.*, vol. 5, pp. 1–7, Oct. 2000.
[60] F. Bouchet and J. Reygner, "Generalisation of the Eyring–Kramers transition rate formula to irreversible diffusion processes," *Annales Henri Poincaré*, vol. 17, no. 12, pp. 3499–3532, Dec. 2016.
[61] L. Gammaitoni, P. Hänggi, P. Jung, and F. Marchesoni, "Stochastic resonance," *Rev. Modern Phys.*, vol. 70, no. 1, p. 223, 1998.

Open Access funding provided by 'Politecnico di Torino' within the CRUI CARE Agreement